Available online at www.sciencedirect.com

ScienceDirect

Acta Materialia 87 (2015) 121–127

Acta MATERIALIA

www.elsevier.com/locate/actamat

Ion-irradiation-induced clustering in W–Re and W–Re–Os alloys: A comparative study using atom probe tomography and nanoindentation measurements

Alan Xu,[a,*] Christian Beck,[a] David E.J. Armstrong,[a] Krishna Rajan,[b] George D.W. Smith,[a] Paul A.J. Bagot[a] and Steve G. Roberts[a,c]

[a] *University of Oxford, Department of Materials, Parks Road, Oxford OX1 3PH, UK*
[b] *Iowa State University, Department of Materials Science and Engineering, Ames, IA 50011, USA*
[c] *Culham Centre for Fusion Energy, Culham Science Centre, Abingdon OX14 3DB, UK*

Received 31 October 2014; revised 19 December 2014; accepted 29 December 2014
Available online 23 January 2015

Abstract—This study examines clustering and hardening in W–2 at.% Re and W–1 at.% Re–1 at.% Os alloys induced by 2 MeV W^+ ion irradiation at 573 and 773 K. Such clusters are known precursors to the formation of embrittling precipitates, a potentially life-limiting phenomenon in the operation of fusion reactor components. Increases in hardness were studied using nanoindentation. The presence of osmium significantly increased post-irradiation hardening. Atom probe tomography analysis revealed clustering in both alloys, with the size and number densities strongly dependent on alloy composition and irradiation temperature. The highest cluster number density was found in the ternary alloy irradiated at 773 K. In the ternary alloy, Os was found to cluster preferentially compared to Re. The implications of this result for the structural integrity of fusion reactor components are discussed.

Keywords: Tungsten rhenium osmium alloys; Nuclear fusion; Atom probe tomography; Ion irradiation; Nanoindentation

1. Introduction

Tungsten is the prime candidate for plasma facing applications in future nuclear fusion reactors, being one of only a handful of materials that are capable of withstanding the harsh operating conditions of up to ~1300 K, power densities of 1–20 MW m^{-2} and irradiation from both 14 MeV neutrons and 2 MeV alpha particles [1,2]. As well as causing large degrees of cascade damage (up to 20 displacements per atom per full-power year) [3], the neutron irradiation will cause pure tungsten to transmute into Re and subsequently Os, yielding potential solute contents as high as 3.8 at.% Re and 1.38 at.% Os after 5 years of reactor operation [4]. Although the equilibrium W–Re–Os phase diagram predicts complete solubility at this composition [5], the mechanical properties of components could be severely degraded due to the formation of irradiation-induced solute-rich clusters as the precursors to sigma and chi precipitates [6,7]. Previous studies of the irradiation responses of these systems are sparse and limited to compositions with more than 3 at.% rhenium and/or osmium present [8–11]. Tanno et al. [8] irradiated W–3Os, W–5Re and W–5Re–3Os in the JOYO Japanese nuclear research reactor. Over a one-year period the alloys were exposed to a neutron dose (>0.1 MeV) of 1.2×10^{26} nm^{-2}, corresponding to 1.54 dpa at ~1032 K, conditions designed to mimic those of the ITER environment [12]. Needle-shaped precipitates were identified by transmission electron microscopy (TEM). Osmium appeared to promote nucleation of precipitates, while Re encouraged their growth [11]. Where Os and Re coexisted in the ternary W–5Re–3Os alloy, Os had a dominant effect, and the precipitation characteristics closely mirrored that of the W–3Os alloy. However, the precipitates were too small to accurately ascertain the compositions and full structures by TEM. Microhardness tests showed increases in hardness in all irradiated samples, with osmium-containing alloys (either binary or ternary) showing a larger increase (up to 8 GPa at 1.54 dpa) than W–Re alloys [11] (up to 5 GPa at 1.54 dpa).

The most detailed chemical characterization of irradiation-induced precipitates in W–Re alloys has been conducted by Herschitz and Seidman [13,14]. Their work used field ion microscopy to image the platelets formed in W–Re alloys post-neutron irradiation. They were able to determine, using 1-D atom probe mass spectrometry, that the precipitates contained either ~50 or ~75 at.% Re. However, the alloys they considered were of much higher

* Corresponding author. Tel.: +44 1865 283658; e-mail: alan.xu@materials.ox.ac.uk

http://dx.doi.org/10.1016/j.actamat.2014.12.049
1359-6462/

rhenium content (10 and 25 at.%) than are currently of interest for fusion applications.

Tungsten ion implantation experiments were performed on a commercial W–5 at.% Re alloy by Armstrong et al. [15] from 0.04 to 33 dpa damage levels at 300 °C. Atom probe tomography (APT) showed that a large increase in hardness above the 13 dpa damage level was associated with the formation of rhenium clusters ~3 nm in diameter, though no study of the composition or density of these clusters was performed.

In this study, ion irradiation was used as an analogue for neutron damage in W–Re–Os binary and ternary alloys. APT was used to study clustering and nanoindentation to measure the mechanical properties of the ion-irradiated layer.

2. Experimental methods

Alloys of W–2 at.% Re and W–1 at.% Re–1 at.% Os and were produced using vacuum arc melting of high-purity powders (Sigma Aldrich and AEE), as described in a previous study [16]. Both alloys were found to have large grain sizes (0.5–2 mm measured via optical microscopy) and to be of high purity (>99.99 at.%, with trace impurities of Al, Si and Ca), as measured using APT and electron probe microanalysis. The ingots were cut into 1 mm thick slices, which were ground and polished with SiC paper and diamond paste. A final colloidal silica (40 nm) finish was used to produce a damage-free surface suitable for implantation and subsequent analysis.

Ion irradiation was performed at the National Ion Beam Centre, University of Surrey, UK. Samples were mounted on a stainless steel temperature-controlled stage (held at either 573 or 773 K) under a vacuum pressure $<10^{-6}$ Pa; for full details see Armstrong et al. [16]. These temperatures were chosen to lie on either side of the stage III vacancy recovery temperature for W of 743 K [17]. A tandem accelerator was used to irradiate the samples with 2 MeV W^+ ions to a fluence of 2.64×10^{15} ions cm^{-2} at a flux of 1.96×10^{10} ions cm^{-2} s^{-1}. A SRIM (stopping range of ions in matter) calculation predicts a damage profile extending to 300 nm below the surface, yielding an equivalent peak damage level of 33 dpa (calculated using the full cascade damage model with a binding energy of 68 eV) [15,16,18].

A dual-beam focused ion beam system (Zeiss Nvision) was used to manufacture lift-out samples for APT analysis pre- and post-irradiation, following procedures described elsewhere [19,20]. Materials were analysed using a Cameca LEAP3000X HR (37% total detection efficiency) in laser mode, running at pulse energies of 0.6–0.8 nJ and a sample stage temperature of 50 K. A minimum of three samples were studied for each alloy and each condition, the data from which were reconstructed using Cameca's IVAS (3.6.6) software.

Nanohardness measurements were made using a Nanoindenter XP (MTS, TN, USA) with a Berkovich diamond indenter calibrated against fused silica. The continuous stiffness measurement mode was used, allowing the hardness to be calculated as a function of depth [21]. The indents were made to 1 μm final depth at a target indentation strain rate of 0.05 s^{-1}, significantly deeper than the 300 nm deep damage layer. Grids of 16 indents were made on each of three different grains at room temperature for each sample and condition. There are difficulties with extracting hardness values from such thin irradiated layers where there will be significant penetration of the plastic zone into the unirradiated material. The method described by Armstrong et al. [15] was used to identify the region in which the hardness of the implanted layer dominates over the unimplanted layer, thus reported hardness values are taken at 125 nm indenter penetration.

3. Results and discussion

3.1. APT analyses

In the unirradiated materials, rhenium and osmium atoms are seen to be homogeneously distributed within the tungsten (see Supporting information for atom maps). The measured solute composition is 1.90 at.% Re in the binary alloy and 1.06 at.% Re/1.11 at.% Os in the ternary (wt.% equivalent to two significant figures). Following ion irradiation, solute clustering was observed in both alloys at both irradiation temperatures, and the level of clustering was seen to vary with implantation depth. This is apparent in Fig. 1a, which shows 4 nm thick sections through an atom map of the W–2Re sample following 33 dpa irradiation at 773 K. The outer surface of the alloy is marked by the carbon layer visible on the left-hand side of the map, below which a region of approximately 200 nm has prominent clustering of Re atoms; at greater depths, the structure returns to being a homogeneous solid solution. Fig. 1b shows the calculated average cluster diameter and volume fraction determined within 10 nm thick bins of the dataset (see below for further cluster analysis details). The cluster volume fraction profile strongly correlates with the damage profile from the SRIM calculation for tungsten at 33 dpa.

To compare the effects of different irradiation conditions/alloy compositions on the microstructures, Fig. 2 shows further 4 nm thick slices over the full set of irradiation conditions and samples, confining the analyses to a depth range of 50–200 nm below the implanted surface, where the peak dose would correspond to 33 dpa.

Fig. 2a shows that the irradiation has induced the formation of a high volume fraction of Re-rich clusters in the binary alloy, approximately 5 nm in diameter. Increasing the temperature to 773 K (Fig. 2b) yields a lower number density of clusters but of larger size, up to 15 nm in diameter. However, this is significantly altered when 1 at.% Os is added to the alloy; at 573 K only slight clustering is noticeable in W–1Re–1Os (Fig. 2c), suggesting that Os is suppressing cluster formation. However, following the 773 K irradiation (Fig. 2d), a high number density of very small (<4 nm dia.) precipitates is formed, enriched in both Re and Os.

To quantify the size, chemical composition and density of clusters observed the maximum separation method algorithm [20] was used to identify and separate any clusters present in the 50–200 nm depth range of each dataset. The method classifies two solute atoms as part of the same cluster if the inter-solute distance falls below a user-defined d_{max} value. Clusters containing fewer solute atoms than a user-specified term N_{min} are rejected to eliminate any small random clustering. An optimum d_{max} value was selected for each irradiation condition/alloy combination based on the procedure proposed by Chen et al. [22] and by Williams

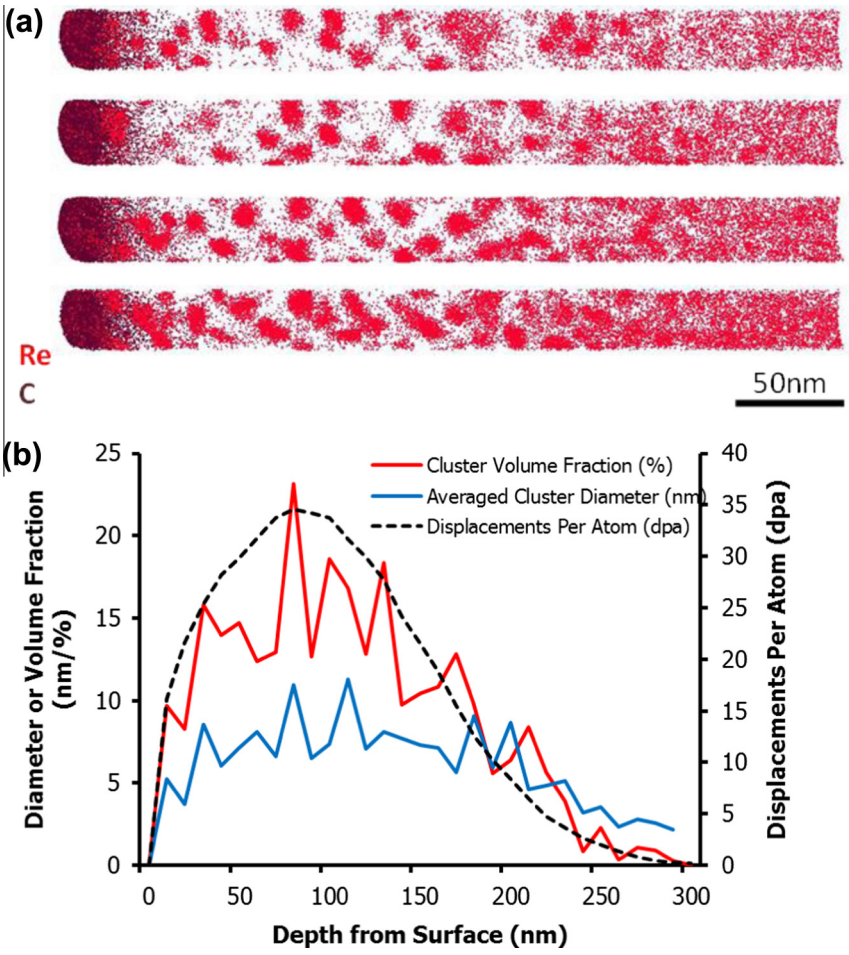

Fig. 1. (a) 4 nm thick slices through the atom map of a W–2Re sample following 33 dpa irradiation at 773 K. Only Re (red) and C (brown) atoms are included, showing Re clustering throughout first 200 nm. (b) Variation of the cluster diameter and cluster volume fraction measured at regular 10 nm slices from the reconstruction. The corresponding dpa level at different depths as predicted by SRIM is also shown. (Color version of figure is available online.)

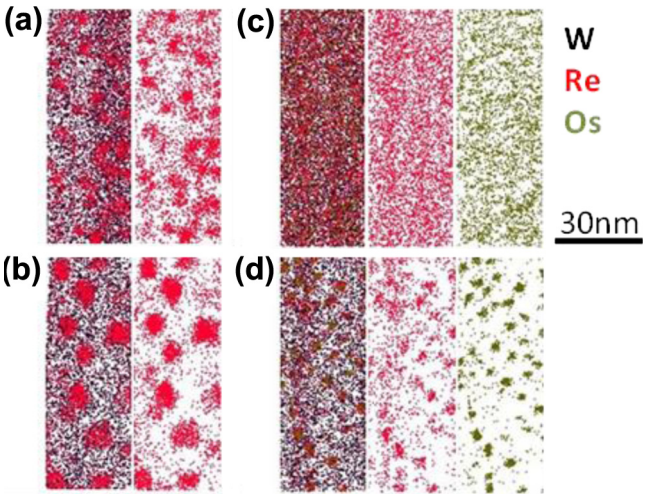

Fig. 2. 4 nm thick sections from atom maps showing species distribution following W–ion irradiation in: (a) W–2Re at 573 K, (b) W–2Re at 773 K, (c) W–1Re–1Os at 573 K and (d) W–1Re–Os at 773 K. W, Re and Os atoms are shown in black, red and green, respectively. (Color version of figure is available online.)

et al. [23]. This method relies on the generation of a nearest neighbour distribution, comparing distances between the clustering species (Re in this case) with those from a randomized data set; d_{max} is selected at a threshold value that excludes randomized clusters from the analysis. Typical d_{max} values used were within the range of 0.9–1.3 nm.

As a complementary method of identifying and isolating clusters, iso-concentration surface analyses were also carried out, with the aim of ensuring that the maximum separation and iso-concentration surface methods yielded similar values for cluster number densities and compositions. The values used for the iso-concentration analyses were determined by picking a level at which the cluster number densities, volume fractions and diameters begin to plateau (6.5 at.% Re, in the case of W–2 at.% Re).

Finally, for the cluster analysis method, an N_{min} value selected using the established protocol of Styman et al. [24]. In this, for the chosen d_{max} value, a cluster size distribution is generated and compared with that from a randomized dataset with the same overall chemical composition. A minimum cluster size (N_{min}) can then be determined by setting a threshold sufficiently high to exclude any wrongly identified random clusters, which in the cases studied here corresponded to a threshold size of

$N_{min} = 20$ detected atoms. Using these optimized values, the resulting figures for cluster compositions, sizes and volume fractions are given in Table 1. The data in each column were averaged over two or three runs under the same alloy/exposure conditions.

At 573 K, the data show a strong segregation of Re in the clusters of the binary alloy, with an average of 8 at.% Re, compared to a bulk value of 2 at.% Re. In the ternary alloy there is no segregation of Re, but instead the clusters are enriched in Os. On raising the irradiation temperature to 773 K, the Re content in the clusters in the binary alloy rises further to nearly 13 at.%. In the ternary alloy there is still little Re segregation to the clusters, while the level of Os rises to nearly 7 at.%. In all cases solute enrichment is accompanied by a slight depletion of the solutes within the matrix, increasing with temperature as cluster formation becomes more marked.

Along with differences in composition, there are also differences in the cluster size distributions with temperature. At 573 K both alloys show similar average cluster radii (2.4 nm in the W–Re alloy, 2.8 nm in the W–Re–Os alloy), but the number densities and volume fractions are higher in the W–2Re alloy. At 773 K significant changes in the cluster characteristics for both alloys are apparent. In W–2Re the average size increases to 3.3 nm, while the number density halves compared to 573 K. In the ternary alloy the size distribution broadens at 773 K, accompanied by a great increase in the number density of the clusters. For both alloys the cluster volume fractions (determined from the cluster average size and number density divided by the reconstructed volume) increase slightly with irradiation temperature, and the ternary alloy has a lower volume fraction.

While the average cluster sizes allow simple comparisons between alloys and irradiation conditions, examining the distribution of sizes obtained gives further insights into the alloy irradiation response. Fig. 3 shows cluster distribution plots for the W–2Re and W–1Re–1Os alloys, with both irradiation temperatures plotted in each. For W–2Re, raising the irradiation temperature reduces the cluster number density; however, Fig. 3) also shows that the similar average cluster sizes reported in Table 1 for W–2Re for both irradiation conditions masks a broadening of the size distribution for irradiation at 773 K. The higher temperature cluster size profile also appears to have a bimodal distribution. W–1Re–1Os responds very differently, however, with a more narrow size distribution that changes only slightly with temperature, as shown in Fig. 3b. The main effect of irradiation temperature is the dramatic rise in cluster number density at the higher temperature (as seen in Table 1).

Proxigram analyses were used to explore the internal chemistry of the clusters as a function of distance from the cores. For each composition and irradiation condition, several similarly sized clusters were isolated using iso-concentration surfaces (set at half the measured cluster compositions reported by the cluster analysis in Table 1). The Re iso-concentration was used for identifying clusters in the binary alloy, whilst the Os iso-concentration was used for the ternary alloy. Averaged proxigrams were then generated for the individual cluster elements, and these are presented in Fig. 4. They show that the Re content of the clusters is significantly higher in the cluster cores than near the shells in W–2Re, particularly so for the alloys irradiated at 773 K. Likewise, the cluster chemistry is non-uniform in the W–1Re–1Os alloy, but in this alloy Os is strongly enriched in the centre of the clusters, again most strikingly at 773 K. The level of Re in the ternary alloy remains low and is consistently within errors across the full cluster profile.

At the higher irradiation temperature in the binary alloy there is evidence for cluster growth, although the full mechanism of the irradiation response needs further detailed study. This is demonstrated in more detail by the change in the shape of the size distributions, where a single peak is observed at 573 K and two peaks are seen at 773 K. The ternary alloy has a slower cluster nucleation rate at 573 K, evident from the lower levels of Os present in the proximity histograms. This nucleation rate increases significantly at 773 K. We suggest that the double peak observed in 33 dpa 773 K W–2 at.% Re is most likely a result of some clusters being dissolved by irradiation and the solute atoms then renucleating as clusters, thus producing the smaller peak in this distribution. The mechanism of radiation-induced dissolution of precipitates and the reprecipitation of fine sub-particles has been studied analytically, e.g. by Frost and Russell [25] and later by Heinig et al. [26], who also used kinetic Monte Carlo methods. This mechanism is predicted to lead to a double peak in the particle size distribution under certain conditions. Experimentally, duplex distributions of coarse and fine precipitates have been observed previously, e.g. by Heinig et al. [26] during the ion irradiation of gold particles in silica and by Monnet et al. [27] in ion-irradiated oxide-dispersion-strengthened ferritic steels.

To explore the kinetics of the clustering in both alloys, the diffusion coefficients for Os and Re in W have been calculated using the Arrhenius equation with D_0 and activation energies values from Ref. [28], which provides values from methods such as the activity of radioactive isotopic solutes diffusing in single crystal tungsten [29]. For Os in W, $D_0 = 0.64 \times 10^{-4}\ m^2\ s^{-1}$ and $E_a = 5.58$ eV; for Re in W, $D_0 = 4.00 \times 10^{-4}\ m^2\ s^{-1}$ and $E_a = 6.18$ eV [28].

These yield D values of $1.8 \times 10^{-58}\ m^2\ s^{-1}$ (Re) and $5.3 \times 10^{-54}\ m^2\ s^{-1}$ (Os) at 573 K, which increase to $2.0 \times 10^{-44}\ m^2\ s^{-1}$ (Re) and $2.7 \times 10^{-41}\ m^2\ s^{-1}$ (Os) at 773 K. These values indicate that diffusion of either alloying addition would be extremely slow if driven by temperature alone. The tungsten ion implantation enhances diffusion via the large number of vacancies produced. Vacancy clusters may also act as nucleation sites for the solute clusters [30–33]. To quantify the extent of diffusion enhancement, we used the methodology of Lescoat et al. [31], which assumes that the particles behave as perfect sinks for point defects to compare these diffusion coefficients. The full mathematical models can be found in the aforementioned reference and are used to derive the irradiation enhanced diffusion coefficients for W–2Re (Re) and W–1Re–1Os (Os) at 33 dpa/573 K, which are 3.24×10^{-29} and $1.40 \times 10^{-24}\ m^2\ s^{-1}$, respectively (we consider Os in the ternary alloy as it is the major clustering species); these values are both nearly 30 orders of magnitude higher than those determined above for thermal-vacancy-mediated diffusion at 573 K. At 773 K, the derived diffusion coefficients are even higher, at 4.99×10^{-26} and $3.69 \times 10^{-23}\ m^2\ s^{-1}$, respectively, for W–2Re (Re) and W–1Re–1Os (Os), which correspond to an enhancement of 18 orders of magnitude compared to thermal-vacancy-mediated diffusion.

There is further evidence in the literature supporting the prominent role of irradiation-produced vacancies in the

Table 1. Cluster characteristics for both alloys at each irradiation condition used.

Cluster feature	573 K 33 dpa W–2Re	573 K 33 dpa W–1Re–1Os	773 K 33 dpa W–2Re	773 K 33 dpa W–1Re–1Os
Re (at.%)	7.99 ± 1.42	1.33 ± 0.40	12.77 ± 2.86	1.88 ± 0.87
Os (at.%)	n/a	4.08 ± 0.70	n/a	6.88 ± 1.57
Radius (nm)	2.39 ± 1.03	2.77 ± 1.36	3.32 ± 1.88	1.93 ± 0.82
Number density (×1000 μm^{-3})	1717 ± 72	1095 ± 56	812 ± 54	2467 ± 112
Volume fraction (%)	9.01 ± 0.38	7.33 ± 0.38	11.21 ± 0.74	9.59 ± 0.44

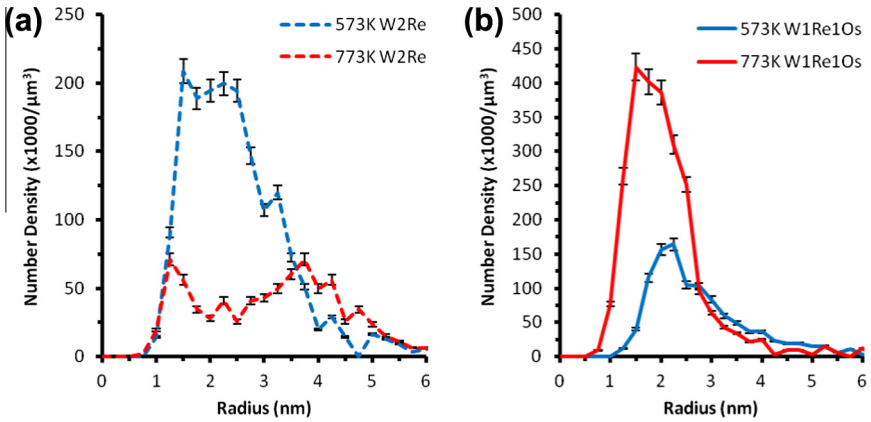

Fig. 3. Cluster size distributions in (a) W–2Re and (b) W–1Re–1Os following ion irradiation at 33 dpa at 573/773 K. (Color version of figure is available online.)

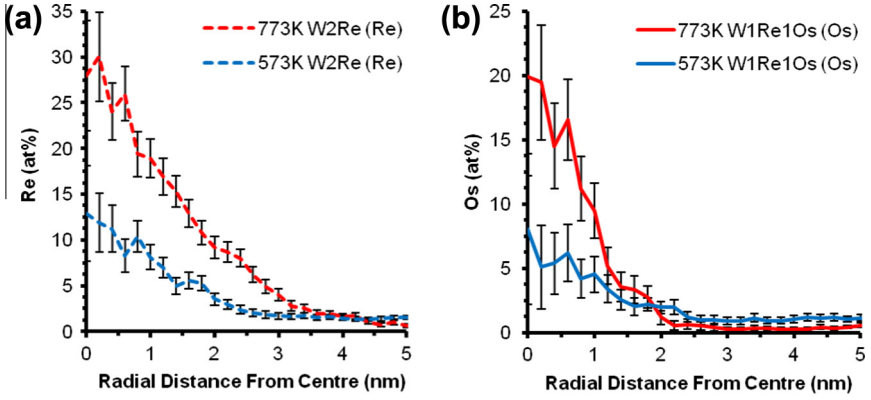

Fig. 4. Proximity histograms through clusters identified in (a) W–2Re and (b) W–1Re–1Os following ion irradiation at 33 dpa at 573/773 K. (Color version of figure is available online.)

alloy's response to irradiation. Becquart and Domain [34] used density functional theory to calculate the Re–vacancy and Os–vacancy binding energies and found them to be 0.2 and 0.35 eV, respectively, indicating that vacancies are more attractive to Os. First-principles calculations by Kong et al. [35] have produced similar values for the binding energies. A possible mechanism therefore is that, for the binary alloy, Re atoms bind to vacancies, which then leads to Re-rich cluster growth as more Re diffuses. This diffusion is likely to be enhanced by local thermal spikes from cascades and the large vacancy population present in the irradiated alloy. In the ternary alloy, Os has a stronger binding energy to vacancies than Re, therefore Os-rich clusters form and subsequently grow, while Re cluster formation is competitively suppressed. In order to discount the possibility that the lack of Re–rich clusters in the ternary alloy was due to the lower Re content, a W–1 at.% Re alloy that had been implanted at 773 K with 2 MeV W^+ ions to 3.6 dpa damage for a separate APT study was also examined. Despite the peak damage experienced being an order of magnitude lower than for the W–1Re–1Os alloy studied here, there is clear formation of Re clusters shown by the Re atom maps in Fig. 6a. These clusters contain an average Re content of 6 at.% and a measured volume fraction of 7.29%. Therefore, a bulk Re content of 1 at.% is adequate to form Re-rich clusters, but the co-presence of 1 at.% Os is sufficient to suppress Re cluster formation, with smaller Os-rich clusters forming instead.

3.2. Irradiation hardening

Nanoindentation hardness measurements taken at an indenter penetration of 125 nm are shown in Fig. 5. The average hardness of the unirradiated ternary alloy is higher

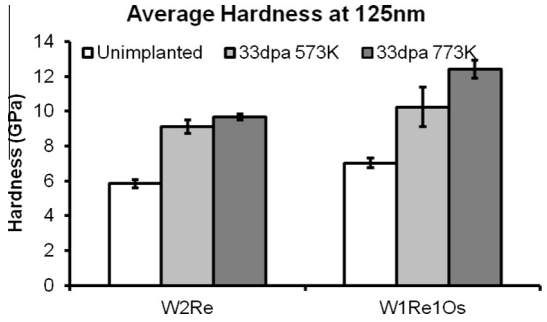

Fig. 5. Nanohardness measured at 125 nm indenter penetration depth for W–2Re and W–1Re–1Os at 573 and 773 K.

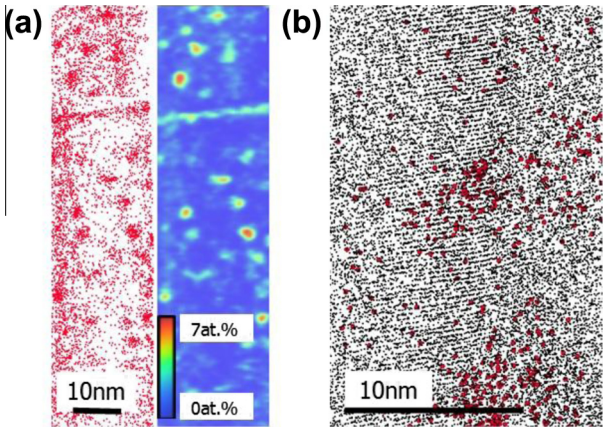

Fig. 6. (a) 4 nm slice of Re atoms from a 3.6 dpa 773 K W^+ ion-irradiated W–1Re alloy. Also shown is the Re concentration contour map. (b) Re clusters in the W–2Re alloy irradiated at 33 dpa at 773 K, demonstrating lattice resolution and coherent clusters along the ⟨1 1 0⟩ pole. (Color version of figure is available online.)

(7.04 GPa) than that of the binary alloy (5.85 GPa). After irradiation at 573 K both alloys show an increase in hardness, of 3.22 GPa in the ternary alloy and 3.27 GPa in the binary alloy, to absolute values of 10.26 and 9.12 GPa, respectively. Following irradiation at 773 K, whilst there is a further increase in hardness in both alloys, it is significantly larger in the ternary alloy, increasing by 5.39 GPa to an absolute value of 12.43 GPa, compared to an increase of 3.84 GPa in the binary alloy to 9.69 GPa. The dramatic rise in the cluster number density seen in W–1Re–1Os following 773 K irradiation is therefore also mirrored in the most pronounced hardness increase being for this alloy.

To assess the strength of the clusters in impeding dislocation motion, an Orowan-type hardening mechanism is assumed, in which clusters harden the material by acting as local obstacles to dislocations, with a strength characterized by a critical breakaway angle ϕ_c [36]. This angle is calculated using the following equation:

$$\Delta\sigma_y = 1.73\frac{Gb}{\lambda}cos\phi_c \quad (1)$$

where G is the shear modulus (161 GPa) and b is the Burgers vector (0.223 nm) [37]. λ is the average distance between clusters minus their diameter, calculated as $[(\rho)^{-\frac{1}{3}} - d]$, where ρ is the cluster number density and d is the average cluster diameter, both of which are taken from Table 1. $\Delta\sigma_y$ is the change in uniaxial yield stress, equal to one-third of the determined hardness values [38]. The factor 1.73 converts from shear yield stress to uniaxial yield stress via the von Mises yield criterion.

Table 2. Calculation of the critical angle that dislocations must subtend in order to pass through clusters.

	ΔH @ 125 nm (GPa)	$\Delta\sigma$ [$\Delta H/3$] (GPa)	λ (nm)	$\Phi_{critical}$ ()
W–1Re–1Os 773 K	5.38	1.79	3.58	84.89
W–1Re–1Os 573 K	3.22	1.07	4.21	86.4
W–2Re 773 K	3.84	1.28	4.13	85.79
W–2Re 573 K	3.26	1.09	3.61	86.67

The critical breakaway angle is found to be ~86° in all alloys (Table 2). This high value indicates that individual clusters are weak obstacles to dislocation motion; the considerable hardening observed is therefore a result of their high density (and thus small spacing, λ). As such, it is likely that dislocations pass individual clusters relatively easily at room temperature by cutting the clusters, rather than by dislocations bypassing the smaller clusters by climb or cross slip. Such a mechanism is promoted by the coherent nature of the clusters with the matrix (see Fig. 6b). It is also possible that vacancies or vacancy clusters that are not associated with clustering could have a hardening effect. The detection of such vacancies or clusters is not possible in APT experiments; however, recent modelling work by Kong et al. [35] suggests that their formation and thus hardening effect should be minimal.

There have been no previous reported results for the irradiation response of such dilute binary or ternary W–Re–Os alloys to such damage levels. However, Tanno et al. [8,11] have reported the effect of neutron irradiation to 1.54 dpa at 673 and 1024 K in W–5 at.% Re and W–5 at.% Re–3 at.% Os alloys. Although the irradiation conditions were different from the current study, they observed similar cluster densities ($2.2 \times 10^6\,\mu m^{-3}$ in W–Re and $6.7 \times 10^6\,\mu m^{-3}$ in W–Re–Os) and radii (1.6 nm in W–Re and 3.4 nm in W–Re–Os) to those observed here. The nanoindentation hardness results presented here are also comparable to the microhardness results obtained by Tanno et al. [11]. They measured an ~11.8 GPa hardness for a W–3 at.% Os alloy neutron-irradiated to 1.5 dpa at 1023 K. Similarly, the W–2 at.% Re exhibited a hardness of 9.34 GPa at 773 K after 33 dpa ion implantation, while in W–5 at.% Re at 1023 K this approached ~9.86 GPa following neutron irradiation. The fact that the cluster size distributions and hardness values are similar despite the significantly higher damage level in the ion-implanted material suggests that the saturation level for the growth of such Re- and Os-rich clusters is at a relatively low damage level.

The different time scales of ion and neutron irradiation may also be also important. Firstly, the higher ion damage dose rate may lead to significantly faster accumulation of damage by ions compared to neutrons, altering the nucleation and growth of the clusters. Such effects have been observed in binary FeCr alloys [39]. Secondly, the total irradiation time in the neutron irradiation is significantly longer, thus allowing more time for diffusion to operate and promoting enrichment of clusters into discrete precipitates. Robust methods to cross-calibrate ion and neutron irradiation experiments are required if ion irradiations are

to usefully inform the design and development of future nuclear systems.

4. Conclusions

In this study, atom probe tomography and nanohardness measurements have offered fresh insights into the phenomenon of irradiation-induced precipitation in W–Re and W–Re–Os alloys. The following major conclusions can be drawn:

- The microstructures developed after ion irradiation in W–Re and W–Re–Os are similar to those produced previously using neutron irradiation.
- Os has a profound effect on the alloy clustering characteristics, almost completely suppressing the formation of rhenium clusters after irradiation to 33 dpa. This is most likely due to Os atoms being more strongly bound than Re atoms to vacancies.
- Individual nanoscale clusters produced are relatively weak obstacles to dislocation motion. Their significant contribution to the hardening in both binary and ternary alloys is due to the large volume fraction present.
- The presence of Os in the ternary W–Re–Os alloy hardens the material significantly after ion irradiation compared to the binary W–Re alloy. The trend matches that of prior neutron irradiation studies. When predicting the mechanical behaviour of tungsten after transmutation in a fusion neutron spectrum, all transmutation products must be accounted for. Using binary W–Re alloys as a reference will cause the likely irradiation hardening to be substantially underestimated.

Acknowledgements

This study was supported financially by the EPSRC under Programme grant EP/H018921/1. We thank the Ames Laboratory for provision of the ternary alloy, the Ion Beam Centre (IBC) at the University of Surrey (a National Facility supported by the EPSRC) for performing implantations and Mr C. Salter (University of Oxford) for supporting the electron probe microanalysis. Prof. M.P. Moody (Oxford University) is thanked for helpful discussions during manuscript preparation. K.R. gratefully acknowledges support from Air Force Office of Scientific Research grants FA9550-11-1-0158 and FA9550-12-0496, and the Wilkinson Chair for Interdisciplinary Engineering at Iowa State University. P.A.J.B. acknowledges travel support from The Queen's College Oxford for an Oxford–Iowa State collaboration. D.E.J. Armstrong is grateful for the funding provided by a Royal Academy of Engineering Research Fellowship.

Appendix A. Supplementary data

Supplementary data associated with this article can be found, in the online version, at http://dx.doi.org/10.1016/j.actamat.2014.12.049.

References

[1] J.W. Davis, V.R. Barabash, A. Makhankov, L. Plochl, K.T. Slattery, J. Nucl. Mater. 258–263 (1998) 308.
[2] M. Rieth, S.L. Dudarev, S.M.G. de Vicente, J. Aktaa, T. Ahlgren, S. Autusch, et al., J. Nucl. Mater. 432 (2013) 482.
[3] B. Raj, M. Vijayalakshmi, P.R.V. Rao, K.B.S. Rao, MRS Bull. 33 (2008) 327.
[4] M.R. Gilbert, J.-C. Sublet, Nucl. Fusion 51 (2011) 13.
[5] P. Villars, A. Prince, H. Okamoto, Handbook of Ternary Alloy Phase Diagrams, ASM International, Materials Park, OH, 1995.
[6] A. Taylor, B.J. Kagle, N.J. Doyle, J. Less-Common Metals 3 (1961) 333.
[7] T. Leonhardt, J. Metals 61 (Issue 7) (2009) 68.
[8] T. Tanno, A. Hasegawa, M. Fujiwara, J.C. He, S. Nogami, M. Satou, T. Shishido, K. Abe, Mater. Trans. 49 (2008) 2259.
[9] H.C. He, A. Hasegawa, M. Fujiwara, M. Satou, T. Shishido, K. Abe, Mater. Trans. 45 (2004) 2657.
[10] J.C. He, A. Hasegawa, K. Abe, J. Nucl. Mater. 377 (2008) 348.
[11] T. Tanno, A. Hasegawa, J.C. He, M. Fujiwara, S. Nogami, M. Satou, T. Shishido, K. Abe, Mater. Trans. 48 (2007) 2399.
[12] K. Tomabechi, Fusion Eng. Des. 8 (1989) 43.
[13] R. Herschitz, D.N. Seidman, Acta Metall. 32 (1984) 1141.
[14] R. Herschitz, D.N. Seidman, Acta Metall. 32 (1984) 1155.
[15] D.E.J. Armstrong, X. Yi, E.A. Marquis, S.G. Roberts, J. Nucl. Mater. 432 (2013) 428.
[16] D.E.J. Armstrong, A.J. Wilkinson, S.G. Roberts, Phys. Scr. T145 (2011) 014076.
[17] D.N. Seidman, Scr. Metall. 13 (1979) 251.
[18] J.F. Ziegler, M.D. Ziegler, J.P. Biersack, Nucl. Instrum. Methods Phys. Res. B 268 (2010) 1818.
[19] M.K. Miller, K.F. Russell, K. Thompson, R. Alvis, D.J. Larson, Microsc. Microanal. 13 (2007) 428.
[20] B. Gault, M. Moody, J.M. Cairney, S.P. Ringer, Atom Probe Microscopy, Springer Science, New York, 2012.
[21] M.C. Oliver, G.M. Pharr, J. Mater. Res. 7 (1992) 1564.
[22] Y. Chen, P.H. Chou, E.A. Marquis, J. Nucl. Mater. 451 (2014) 130.
[23] C.A. Williams, D. Haley, E.A. Marquis, G.D.W. Smith, M.P. Moody, Ultramicroscopy 132 (2013) 271.
[24] P.D. Styman, J.M. Hyde, K. Wilford, G.D.W. Smith, Quantitative methods for the APT analysis of thermally aged RPV steels, Ultramicroscopy 132 (2013) 258–264.
[25] H.J. Frost, K.C. Russell, Acta Metall. 30 (1982) 953.
[26] K.H. Heinig, T. Muller, B. Schmidt, M. Strobel, W. Moller, Appl. Phys. A Mater. Sci. Process. 77 (2003) 17.
[27] I. Monnet, P. Dubuisson, Y. Serruys, M.O. Ruault, O. Kaitasov, B. Jouffrey, J. Nucl. Mater. 335 (2004) 311.
[28] G. Neumann, C. Tuijn, Self-Diffusion and Impurity Diffusion in Pure Metals, Elsevier, Oxford, 2009.
[29] N.K. Arkhipova, S.M. Klotsman, I.P. Polikarpova, G.N. Tatarinova, A.N. Timofeev, L.M. Veretennikov, Phys. Rev. B 30 (1984) 1788.
[30] Z.W. Zhang, C.T. Liu, X.L. Wang, M.K. Miller, D. Ma, G. Chen, J.R. Williams, B.A. Chin, Acta Mater. 60 (2012) 3034.
[31] M.L. Lescoat, J. Ribits, Y. Chen, E.A. Marquis, E. Bordas, P. Trocellier, Y. Serruys, A. Gentils, O. Kaitasov, Y. de Charlan, A. Legris, Acta Mater. 78 (2014) 328.
[32] J.N. Mundy, S.J. Rothman, N.Q. Lam, H.A. Hoff, L.J. Nowicki, Phys. Rev. B 18 (1978) 6566.
[33] R.L. Danilowicz, Point Defect Calculations in Tungsten. NASA Technical Note TN D-4918, NASA, Cleveland, OH, 1968, p. 15.
[34] C.S. Becquart, C. Domain, Curr. Opin. Solid State Mater. Sci. 16 (2012) 115.
[35] X.S. Kong, X. Wu, Y.-W. You, C.S. Liu, Q.F. Fang, J.-L. Chen, G.-N. Luo, Z. Wang, Acta Mater. 66 (2014) 172.
[36] R. Abbaschian, L. Abbaschian, R.E. Reed-Hill, Physical Metallurgy Principles, fourth ed., Cengage Learning, Stamford, CT, 2010.
[37] S.W.H. Yih, C.T. Wang, Tungsten: Sources, Metallurgy, Properties and Applications, Plenum Press, New York, 1979.
[38] M.F. Ashby, D.R.H. Jones, Engineering Materials 1: An Introduction to Properties, Applications & Design, Butterworth–Heinemann, Oxford, 2012.
[39] C.D. Hardie, C.A. Williams, S. Xu, S.G. Roberts, J. Nucl. Mater. 439 (2013) 33.